Advanced Detector Signal Acquisition and Electron Beam Scanning for High Resolution SEM Imaging

William C. Lenthe[1,a,b], Jean Charles Stinville[a], McLean P. Echlin[a], Zhe Chen[a], Samantha Daly[c], Tresa M. Pollock[a]

[a]*Materials Department, University of California Santa Barbara, Santa Barbara, California 93106-5050*
[b]*Materials Science and Engineering, Carnegie Mellon University, 5000 Forbes Avenue Wean Hall 3325, Pittsburgh, PA 15213*
[c]*Mechanical Engineering Department, University of California Santa Barbara, Santa Barbara, California 93106-5050*

Abstract

The advancement of materials science at the mesoscale requires improvements in both sampling volumes/areas and spatial resolution in order to make statistically significant measurements of microstructures that influence higher-order material properties, such as fatigue and fracture. Therefore, SEM-based techniques have become desirable due to improvements in imaging resolution, large sample handling capability, and flexibility for in-situ instrumentation. By using fast sampling of SEM electron detector signals, intrinsic beam scanning defects have been identified that are related to the response time of the SEM electron beam deflectors and electron detectors. Mitigation of these beam scanning defects using detector sampling approaches and an adaptive model for settling time is shown to produce higher resolution SEM images, at faster image acquisition times, with a means to quantify the different response functions for various beam deflectors and detectors including those for electrons and ions.

Keywords: scanning electron microscopy, high resolution digital image correlation, scan generator, SEM, imaging defects, image processing

1. Introduction

Scanning electron microscope (SEM) instruments have become increasingly important for the characterization of materials at the mesoscale. SEMs are ideal for in-situ experiments where instrumentation can be volumetrically large (mechanical tests) and operate at high temperatures (heating) or at low temperatures (coolants or cooling stages) that require resilient vacuum systems. Furthermore, the mechanisms that drive events such as deformation and slip often occur over short timescales, and therefore require fast imaging modes with short loading hold times or continuous loading in order to mitigate structural relaxations that are particularly evident at elevated temperature. For instance, emerging high resolution scanning electron beam technologies have enabled the imaging of defects via SEM scanning transmission electron microscopy (TSEM) [1–3], and SEM digital image correlation (DIC) techniques for the measurement of strain at the micron to sub-micron scale [4–7]. Recent experiments have also combined in-situ capabilities including heating stages with mechanical loading [8–11].

Scan field distortions and beam scanning defects have been identified during the development of high-resolution SEM DIC techniques for the measurement of elastic and plastic strains at the grain and subgrain scale [4–7, 12–14]. Furthermore, increasing the electron beam dwell times at each pixel can produce sample charging and beam drift. SEM DIC is limited in its displacement resolution by the quality of the unique fiducial marks or speckle pattern being tracked and the minimum resolvable feature sizes. Therefore, reducing dwell time and enhancing imaging resolution will result in improvements in displacement resolution in the SEM DIC technique. Presently, we show that a fast analog and digital input/output (IO) controller can be used to scan the SEM beam while fast sampling the detector signals, in order to improve image acquisition speed while maintaining resolution by using image correction algorithms. The custom signal acquisition system was used to investigate the influence of imaging conditions and hardware on the overall system response time.

2. Background

Modern SEMs generally use either a high current ($>1\,\mu A$), lower brightness tungsten filament electron emitter or a field emission gun (FEG) that provides up to $0.1–0.5\,\mu A$ of current with much higher brightness. The electron beam generated by these emitters is focused through a series of electromagnetic lenses and apertures to produce a tightly focused spot on the sample surface, with a specific accelerating voltage and beam current. The probe is scanned across a sample surface using either electrostatic plates or electromagnetic coils. Electrostatic plates deflect the beam faster than electromagnetic coils, but they are more susceptible to stray field interference if improperly shielded [15, 16].

Electromagnetic coils can be approximated coarsely by an

☆

*corresponding author
Email addresses:* `wlenthe@andrew.cmu.edu` (William C. Lenthe), `mechlin@ucsb.edu` (McLean P. Echlin)

inductor with the magnetic field

$$B = \mu_o \frac{N}{L} I \qquad (1)$$

where μ_o is the permeability of free space, N the number of coil turns, L the coil thickness, and I the current. The radius of curvature of an electron traveling perpendicular to a magnetic field is

$$r = \frac{mv}{qB} \qquad (2)$$

where m is the particle mass, v the particle velocity, and e the electron charge. Moving through a uniform magnetic field of thickness L will deflect an electron by the angle

$$\theta = \arcsin \frac{L}{r} \qquad (3)$$

The deflected distance of the electron (ignoring the deflection within the field) is

$$x = w \tan \theta \qquad (4)$$

where w is the distance from the coil to the sample. Replacing velocity with kinetic energy $v = \sqrt{\frac{2K}{m}}$ and assuming small deflection angles ($\tan \theta \approx \arcsin \theta$) the deflection at the sample can be approximated

$$x \approx \frac{wq\mu_o NI}{\sqrt{2Km}} \propto \frac{I}{\sqrt{K}} \qquad (5)$$

Similarly, electrostatic deflectors can be approximated by a parallel plate capacitor with an electric field

$$E = \frac{V}{d} \qquad (6)$$

where V is the voltage between plates and d is the spacing. Assuming small deflection angles an electron spends

$$t \approx \frac{L}{v} \qquad (7)$$

traveling through the plates where v is the speed of the electron and L is the field thickness. Since the force on an electron in an electric field is $f = eE$ the final speed perpendicular to the plates is

$$v_\perp = \frac{f}{m} t = \frac{eVL}{dmv} \qquad (8)$$

assuming $v_\perp \ll v$ (small deflection angles) the deflection at the sample can be approximated

$$x \approx w \frac{v_\perp}{v} \approx \frac{weVL}{dmv^2} = \frac{weVL}{2dK} \propto \frac{V}{K} \qquad (9)$$

If the scanning system is modeled as a simple resistorinductor (RL) or resistor-capacitor (RC) circuit, moving the beam from one point to another invokes a current or voltage impulse response respectively. According to Equation 5 and Equation 9 the effect of magnification should be similar for both systems with high magnifications requiring smaller steps (smaller impulses) and in turn shorter transients (faster settling times).

Similarly both systems will require larger impulses at higher accelerating voltages and therefore longer transients with electromagnetic coils and electrostatic plates having an inverse square relationship linear inverse dependence respectively.

Many different detectors are implemented in modern SEM systems. An example is a standard secondary electron detector (Everhart-Thornley detector (ETD)), which utilizes a biased cage to accelerate low energy electrons towards a phosphor that is imaged through a light guide with a photomultiplier tube [17]. Amplified solid state silicon detectors are also used, such as a backscatter detector [18–20] or a transmission type TSEM detector [1–3], which allow for imaging of higher energy electrons that are either backscattered or transmitted from or through the sample. The response times of detectors can not be modelled as simply as beam deflectors, but response and recovery times may vary based on the detector design, material, and electronics [21–23].

SEM manufacturers employ a range of beam scanning methodologies, which typically aim to achieve the same goal of shifting the beam along an X–Y grid with incremental discrete dwell spots regularly spaced in both directions. For instance, the FEI microscopes used in this study utilize a scan generator with the X-axis signal incrementing from X=0 to X_{max} with a finite step dX, before incrementing the Y-axis signal by dY and then repeating the X=0 to X_{max} scan with the discontinuity between lines sometimes referred to as flyback or jumpback. We refer to this scan pattern as a raster scan and it is shown schematically in Figure 1(a). Incrementing X for even lines and decrementing X for odd lines with dY increments at each end of line eliminates the discontinuity as shown in Figure 1(b) and will be referred to as a snake scan.

In a conventional SEM, as the deflectors incrementally steer the beam to discrete (X,Y) positions on the sample surface and measure the detector response at each point to form an image. Most SEMs allow frame or line integration where the same region or line is imaged multiple times and averaged to reduce noise. Aligning images before integration allows mitigation of drift but typically requires manually saving individual images and post-processing. Even collecting images without frame or line integration implements pixel integration with multiple detector samples from the duration of the dwell time averaged into a single value. Formation of an image by signal integration assumes that the overall system response time is fast compared to collection speeds (either detector, line, or frame speeds for pixel, line, or frame averaging respectively). A custom external scan controller and fast (2.0 MS/s) detector signal acquisition permits the collection of unintegrated images with multiple samples per pixel to measure and correct for system response time.

3. Experimental procedure

3.1. Material

A thermally treated, polycrystalline, powder metallurgy processed, nickel-base superalloy René 88DT was used due to the high imaging contrast of the sub-micron distributions of γ'
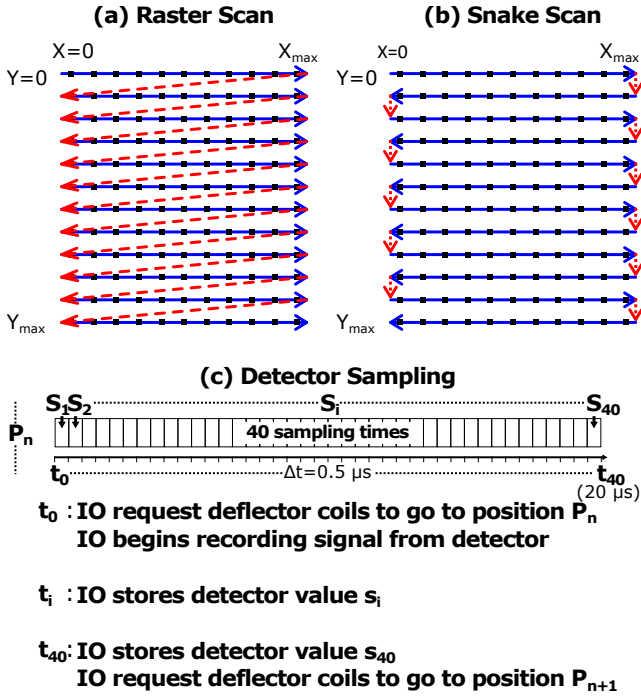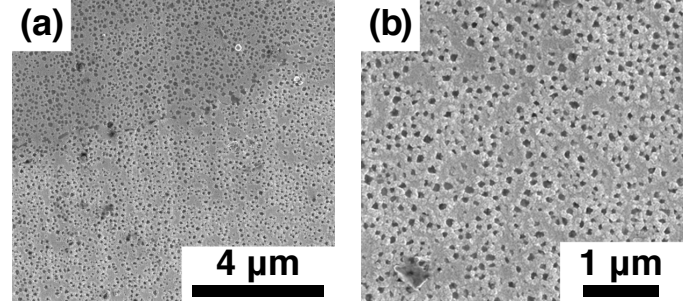
Figure 2: (a) An oxidized polycrystalline nickel-base superalloy sample surface shows a high contrast random sub-micron scaled speckle pattern and grain orientation contrast. (b) A higher magnification image shows detail of the speckle pattern. The random speckle pattern on this material is used to make DIC comparisons between image sets from identical sample locations.

secondary phase precipitates [24, 25], which act as a natural speckle pattern. These precipitates range from 100–200 nm in diameter and are slightly oxidized, due to a thermal treatment, to achieve high imaging contrast [4].

This René 88DT alloy has been used in a series of previously reported high resolution SEM DIC strain measurement studies with 0.15% strain resolution and sub-micron spatial resolution [4, 14, 26]. The microstructure of the fine-scaled and equiaxed random speckle pattern of the oxidized secondary gamma prime precipitates is shown in Figure 2. The oxidized gamma prime particles at the sample surface are strongly adhered, non-charging, and stable at least to $650°$C [26].

Two phase Ti-6Al-4V was also investigated in this study. The Ti-6Al-4V material has microtextured regions resulting from the rolling processing steps and an equiaxed $\alpha - \beta$ microstructure resulting from the mill annealed condition. These samples were prepared by lightly etching the surface using Kroll's reagent for 15 seconds [27], which results in a µm-scale speckle pattern that was used to investigate imaging stability.

3.2. Experimental Techniques

Images were collected on a FEI Versa 3D FIB-SEM and a FEI Helios FIB-SEM microscope over a range of accelerating voltages, beam currents, and magnifications. Fields of view were selected to balance lens and drift distortions [28]. The stock secondary electron detectors (ETDs) were used on both instruments, and an insertable back scattered electron (BSE) detector was used on the FEI Versa 3D microscope. Electron beam scanning was controlled using the integrated microscope scan components and a custom beam scanner setup connected to the external scan control port on each microscope. The custom beam scanner consists of a fast digital/analog 16-bit IO controller (National Instruments NI-DAQ 6363) and C++ based beam scanning software available in an online repository (https://github.com/PollockGroup/ExternalScanControl). Images of the controller and the wiring schematic used to interface with the microscope are shown in Figure 3. Two analog outputs were used to send horizontal (X-axis) and vertical (Y-axis) scan signals to the microscope with a voltage range of ±4.0 V and a resolution of 122 µV and sample rate of 2.86 MS/s. Analog

Figure 1: Raster (a) and snake (b) beam scanning patterns are shown schematically. The simultaneous Y-axis increment and reset of X back to X=0 position in (a) is often called flyback or jumpback, and is the typical scan method for most FEI microscopes. 40 samples (c) were collected from the detector using a custom IO controller at 0.5 µs intervals over a 20 µs dwell at each desired position P_n on the scan pattern in (a) or (b). A set of 40 images (4096 × 4096 pixels) was formed from each of the associated 0.5 µs sampling intervals.
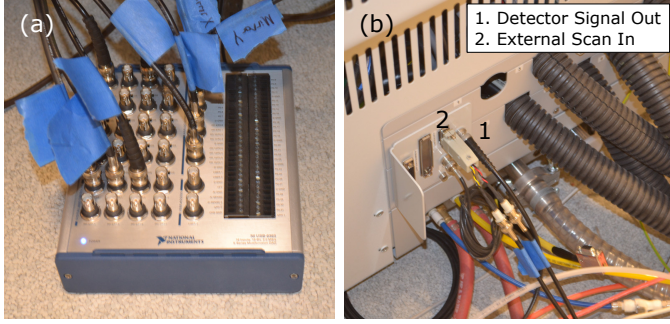
Figure 3: (a) The high speed (2.0 MS/s) National Instruments analog and digital IO controller used to sample the detector signals and produce the SEM deflector scan voltages. The analog input controller samples the secondary electron and backscatter electron detector signals at at rate of 0.5 μs/sample, while producing the scan signal, all with a synchronized hardware bus. (b) The electron beam scan input port that exists on most FEI SEM microscopes was used to bypass the stock scan controller and directly apply voltages to a signal amplifier and then to the beam deflectors.

inputs were used for fast sampling of the secondary electron detector (ETD) signal and the backscatter electron detector. The analog inputs on the NI-DAQ 6363 are capable of 2.0 MS/s (sampling at 0.5 μs).

Typically, image acquisition using FEI microscopes is performed by designating a scan (imaging) resolution, a dwell time at each pixel, and a magnification (the horizontal field width). The scan generator then places the beam at each pixel location for the specified dwell time with a raster scan pattern. Using the custom scan code and generator, the scan pattern and sampling interval of the detector signal can be arbitrarily modified, but only raster and snake patterns were considered for this study.

During each individual pixel dwell, the detector signal is sampled at a rate of 2.0 MS/s. Images collected using the custom IO controller are composed from a series of 20 μs beam dwells at each location P_n with measurements collected every 0.5 μs for 40 measurement at each pixel. The 40 unique samples at each P_n are stored in an array instead of averaging, enabling measurement of and correction for system response time. A relatively long 20 μs dwell time was used to ensure the system stabilized by the end of each pixel and because it is representative of SEM DIC techniques which are particularly sensitive to image distortions [29].

4. Results

The new scanning hardware and software allows for sampling of detector data at fast rates and analysis of the collected data as fully independent samples. While monitoring the detector signals, the electron beam deflectors can be scanned, while maintaining a synchronized hardware system clock. Examination of the time resolved detector data reveals when the system stabilized, with the following caveats: (1) the sampling rate must be faster than the beam scan dwell time (fractional μs-scaled) and (2) the total sampling time must be long enough such that the imaging instabilities stabilize/converge. If these conditions are satisfied, then the rate and time of system stabilization can be determined by comparison of the initial and fi-

nal samples. System stabilization profiles was measured using SEM DIC [14] and a fast Fourier transform (FFT) based image registration algorithm [30] to quantitatively determine the pixel displacements as a function of time.

In the subsequent sections, the settling time is determined using the displacement field algorithms described. Furthermore, the functional dependency of the imaging stability on electron beam parameters compared to detector parameters was investigated by comparing the signals and response times at a wide variety of beam conditions and with both secondary electron and backscatter detectors. Using the new insights on the factors that influence system stabilization times, a model and algorithm is presented that allows measurement of and correction for settling time. This approach can be used to improve feature sharpness (imaging resolution), while maintaining the improved imaging contrast that results from longer pixel dwell times.

4.1. Vertical (Line Jump) Errors

The SEM DIC technique [14] and commercial DIC software [31] was used to measure the displacement and strain fields between undeformed image pairs using the FEI microscope scan controller and the custom IO scan controller. The displacement field measured for a given image pair shows the location of non-systematic image defects, such as line scan defects shown in Figure 4(a), that occur when the electron beam is deflected in too large or small of an increment in the Y direction (vertical). These errors are attributed to the vertical line jumps, in red, that occur during execution of the scan patterns shown in Figure 1. An otherwise identical SEM image was formed using the custom scan controller with a snake scanning pattern, resulting in improved Y direction beam step stability in Figure 4(b). Figure 4(c) shows the custom scan controller decreases the strain magnitude of large errors by a factor of 2–3 X.

4.2. Horizontal (Scanning Direction) Errors

Defects that occur in the direction of travel for horizontal line scanning are difficult to perceive because the raster scan method implemented in Figure 1(a) produces global shifts that affect all the features being imaged. However, when scanning is performed using the snake scanning method in Figure 1(b), the horizontal line shifts are in different direction on alternating lines, making them more apparent, as shown in Figure 5(b & e). The shift is an artifact of slow electron beam deflection and detector latency resulting in a system response time that is large compared with the sampling speed. The animated image sequences in the Supplemental Figure section show imaging data from experiments where the system settles as a function of time, which can be seen as a global shift in the image during raster scanning and as the transformation of ragged particle edges into sharp particle edges during snake scanning. Each image is composed of thousands of individual stabilization experiments where the sampled volume shifts from the prior pixel location to the next pixel location in the scan. Since the prior pixel location is determined by the scan pattern, the systematic shifts change as a function of the scan type.

(a) Microscope Scan Controller **(b) Custom Scan Controller**

(c) Difference in ε_{yy} Intensity

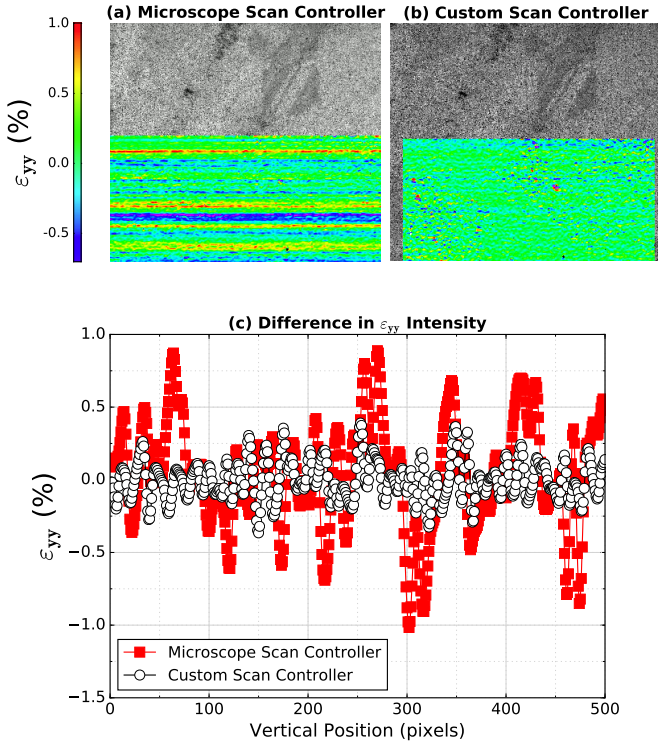Microscope Scan Controller
Custom Scan Controller

Figure 4: Identical regions of the nickel sample were imaged in pairs using (a) the stock FEI microscope scan controller and (b) the custom external scan controller. The ϵ_{yy} strain field shows that the the custom controller produces fewer and smaller magnitude vertical (Y direction) line jumps or instabilities. An ϵ_{yy} line plot extracted at the same vertical location using the stock scan controller (a) and the custom external scan controller (b) is shown in (c) indicating the difference in amplitude and frequency of instabilities.

Experiments were performed using the custom scan controller to collect detector information using the snake scan pattern with a $20\,\mu s$ dwell time at each pixel for 4096×4096 resolution maps. The ETD signal was sampled at $0.5\,\mu s$ intervals to build image datasets that can be analyzed as a function of settling time. On a conventional SEM, the detector intensity is averaged or integrated over the requested dwell time for each pixel. For instance, when the detector intensity for the entire $20\,\mu s$ dwell is averaged for each pixel position then the pixel shifts are subtle, as shown in Figure 5(a). However, if a shorter imaging dwell time is chosen by averaging the first $5\,\mu s$, then the image in Figure 5(b) has ragged edges where neighboring pixels locations are being partially sampled. The slow system stabilization effect can be removed by omitting the initial detector data, for instance, averaging the signal from 10–$15\,\mu s$ as shown in Figure 5(c). The edges in Figure 5(c,f) are sharper than those in Figure 5(a,d), although the contrast in Figure 5(c,f) is lower due a dwell time that is only 25% as long.

The settling effect is most pronounced when the snake scanning pattern is used, due to the apparent shifts between the alternating scan direction lines. This effect is still present when the raster scanning pattern is used, but not as obvious because all scan lines shift in the same direction. The two types of imaging artifacts present in raster and snake scanning are shown in Figure 6, where the interlaced shifts are between (b) & (d) and the consistent image shifts are between (a) & (c). The imaging artifacts are small, but reduce the sharpness and the contrast of features present in high resolution SEM imaging, such as the edge of the small particle shown in Figure 6 or the precipitate microstructure in Figure 5.

4.3. Quantitative Measurement of System Stabilization Time

The custom scan controller was used to fast sample from the SEM detectors to gather image datasets. The datasets were investigated using two methods to measure pixel displacements as a function of time. SEM DIC [6, 7, 14, 32, 33] provides displacement field data and measures strain by tracking subsets of unique fiducials on the sample surface, in this case, the oxidized precipitates. Shifts were computed by creating an image for each sample (e.g. 40 images from the samples shown in Figure 1(c)), performing a DIC calculation using the final sample image as the reference, and averaging the displacements across all subsets. Also, an FFT based registration algorithm was used to align the sequence of images [30]. Shifts were computed row by row for the FFT method and averaged, enabling application to both raster and snake scan patterns. Sub-pixel displacements were tracked using both the SEM DIC and FFT image registration approaches, showing systemic shifts that can be tracked as a series of individual beam stabilization experiments in order to determine the response time. Measurements of shifts using the SEM DIC and FFT image registration methods as a function of detector sampling time for a time-based imaging datastack are shown in Figure 7. Both methods capture the same image displacements as a function of time.

The FFT technique was used to measure overall system response time as a function of SEM parameters shown in Figure 8

Detector Signal Averaged Over:

t = 0 to 20 µs　　　　　t = 0 to 5 µs　　　　　t = 10 to 15 µs
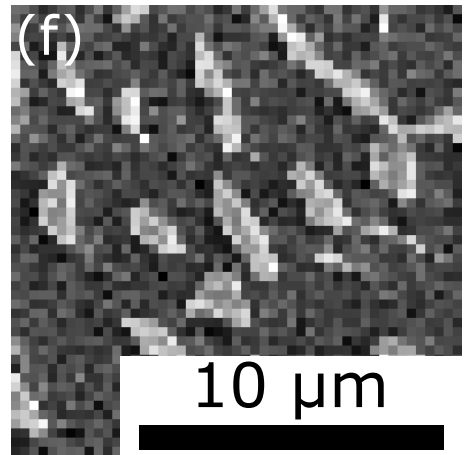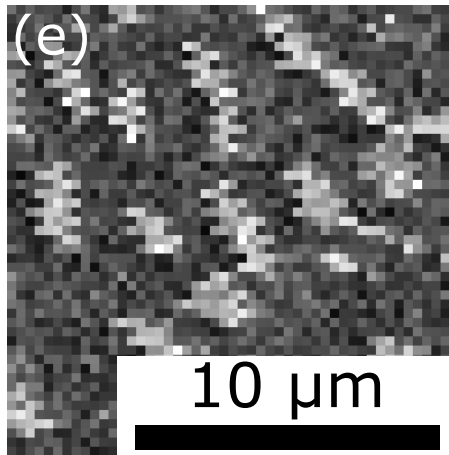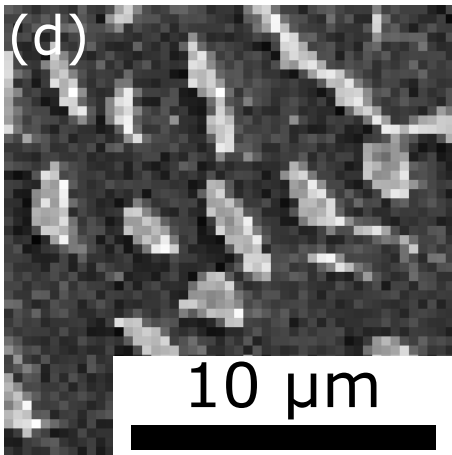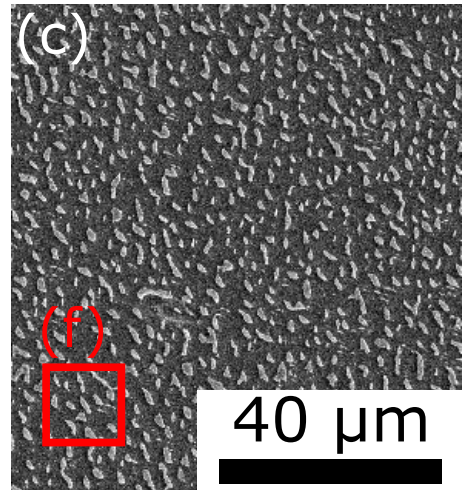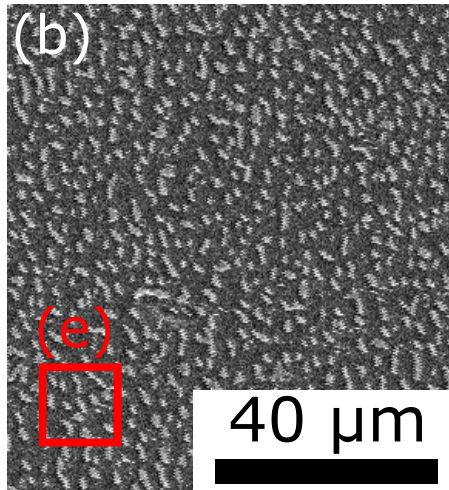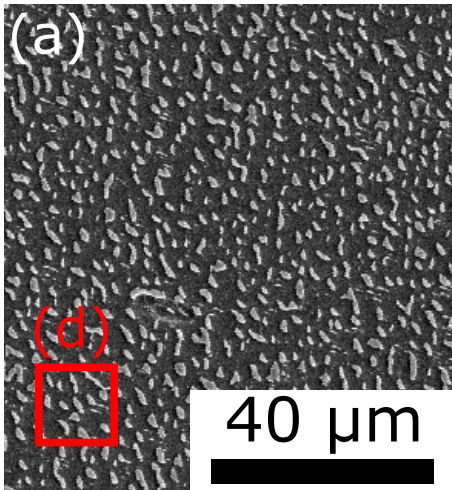

Figure 5: The custom scan controller was used to collect 20 µs of total dwell time from each pixel location using snake and raster scan patterns on the nickel alloy. The controller simultaneously deflects the beam to the next pixel location and begins reading from the ETD at 0.5 µs intervals. The detector values over each interval are individually saved instead of averaging, permitting them to be subsequently averaged for arbitrary subintervals as shown. Beam sampling from adjacent horizontal (X) pixel locations is visible in the 0–5 µs interval. Averaging over 10–15 µs, the beam has stabilized at the target beam/pixel location and forms a sharp image. If the entire dwell interval is averaged (0–20 µs), then the early time effects while the detector and beam are sampling from the adjacent pixels is mostly averaged out by the stabilized imaging that occurs at later times.
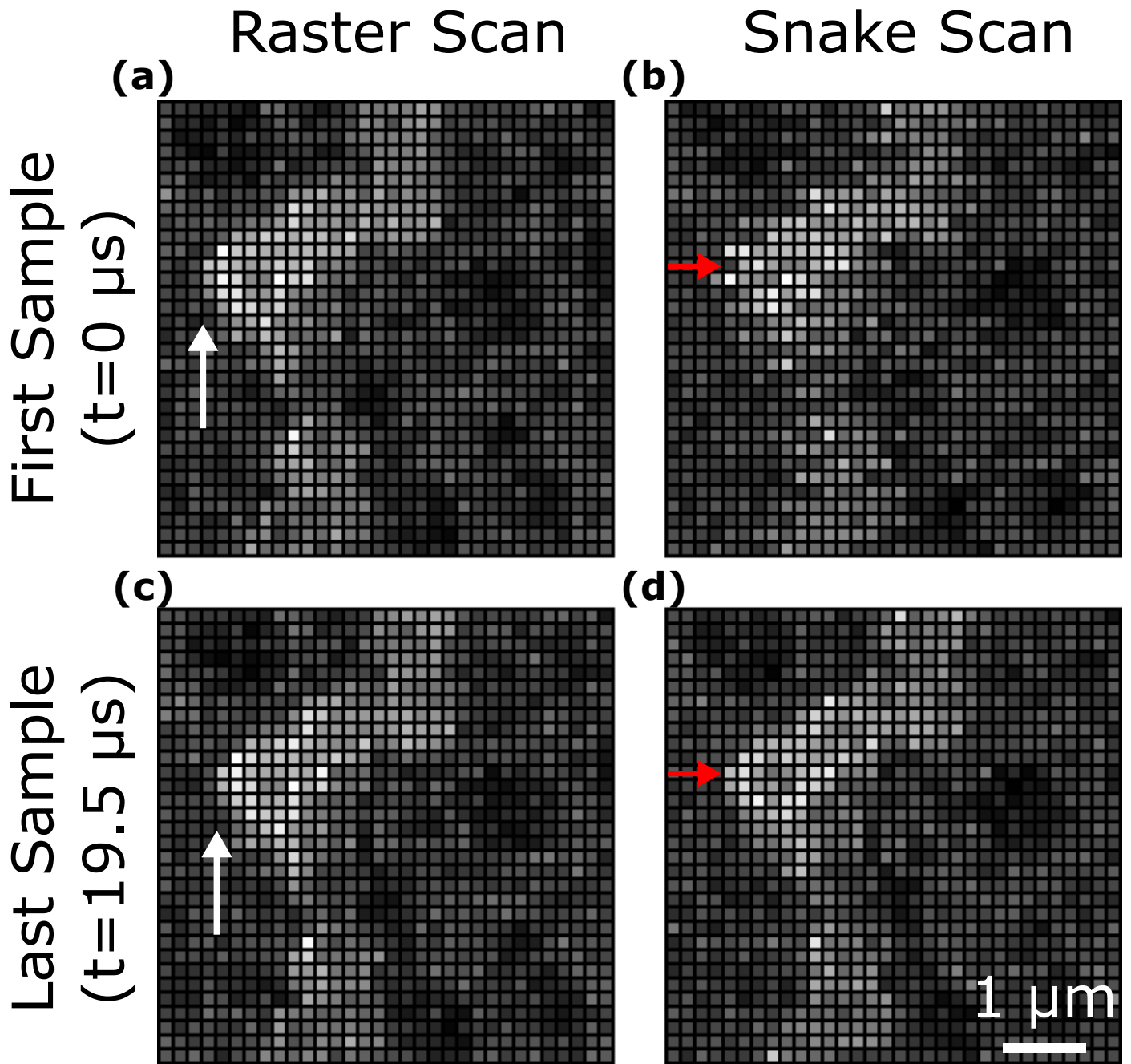
Figure 6: SEM images of a particle on the nickel alloy (particle: white, γ phase: light gray, γ' phase: dark gray) imaged with a 20 kV electron beam. 40 samples of 0.5 μs length were collected during a 20 μs total dwell. The identical sample region was imaged with raster scanning on the left (a, c) and snake scanning on the right (b, d). Scan patterns show a one pixel shift when comparing the first sample at each pixel (a, b) to the last sample at each pixel (c, d). In the raster scanning images, the entire particle shifts 1 pixel (white arrows indicate the particle's left edge). On the snake scanning images, the shift is more pronounced because every other line is shifted in opposite directions (red arrows highlight image tearing). The images shown are 32 × 32 pixel sub-regions extracted from the center of larger 4096 × 4096 pixel images.
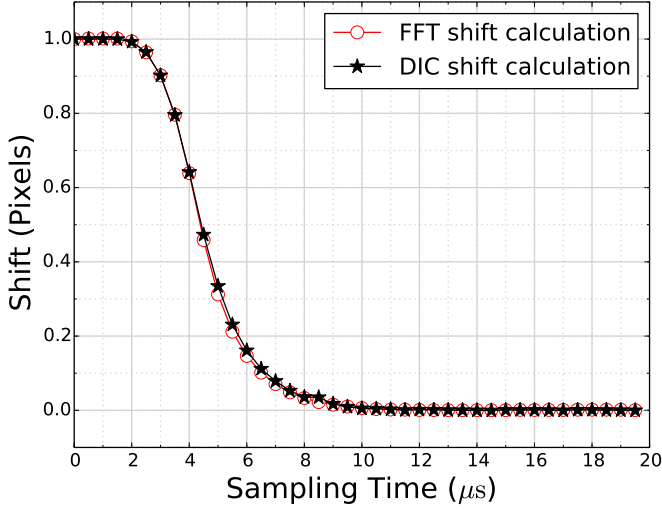
Figure 7: Image displacements were measured as a function of detector sampling time for time-based imaging datastacks using both the SEM DIC and FFT image registration methods. Both methods capture the sample pixel displacements as a function of time.

including (a) beam deflector type, (b) beam accelerating voltage, (c) detector type, and (d) imaging magnification. The system response time with electrostatic deflectors is roughly half the response time with electromagnetic deflectors as shown in Figure 8(a), system response time increases with increasing accelerating voltage and magnification as shown Figure 8(b,d), and the response time of a solid state BSE detector is significantly slower than an ETD as shown in Figure 8(c).

4.4. Correcting Imaging Displacements

Displacements occur due to a combination of column and detector response time which are in turn a function of imaging condition, making the precise prediction of shifts difficult without a complete physics based model. However, if a custom scan controller is used to fast-sample the detector signal, then the shifts can be computed and corrected by post processing or in real time regardless of their origin. The fast-sampled image dataset shown in Figure 5 was corrected by measuring a system stabilization response function such as those shown in Figure 8, and applying the shifts to each pixel for the entire image stack. The averaged uncorrected images, and the resulting shift-corrected and averaged image dataset, are shown in Figure 9.

Shifts may be calculated from a fit curve to correct for scatter arising from noisy, small, or low contrast images. Dwell times long enough for the system to stabilize generally have an asymmetric sigmoidal shape and can effectively fit with a Gompertz type curve of the form:

$$\text{shift}(t) = 1 - \exp\left(-b \exp\left(-ct\right)\right) \tag{10}$$

where b controls the fit of the time, $t_{1/2}$, for a shift of ½ pixel and c controls the fit of the maximum shift derivative, d_{max}, according to the relationships $c = -\ln\left(ln(2)/c\right)/t_{1/2}$ and $d_{max} = c/e$. A Gauss-Newton algorithm to compute the least squares fit curve for a set of shifts is included with the scanning code.

4.5. Discussion

Two major SEM electron beam scanning artifacts were identified: (1) vertical line jump precision errors occurring between horizontal line scans, and (2) system stabilization errors that occur due to SEM imaging parameters and microscope hardware response time. The frequent vertical line jump precision errors can be significantly reduced by incorporating a high resolution, high speed IO controller and using a snake scanning pattern. Larger, less frequent jumps, potentially due to charging particles within the electron column, have been reported and specialized algorithms developed for their detection and correction [12]. Access to time resolved detector samples may provide an avenue for more sophisticated measurement and mediation of these and other scanning related artifacts. Stabilization errors can be mitigated by measuring and correcting for the system response time if time resolved detector samples are collected.

Deconvolving the contribution of individual system components to the overall response is not always possible, but general trends can provide some insight. The system response time of the FEI Helios microscope with electrostatic deflectors is roughly half the response time of the FEI Versa 3D microscope with electromagnetic deflectors for the same imaging conditions, suggesting that the electrostatic deflectors have a faster response time than the electromagnetic deflectors. The system response time with an ETD is significantly faster than with a solid state BSE detector allowing measurement of smaller changes. Increasing accelerating voltage causes a small but measurable increase in settling time, consistent with the impulse response of an inductor or capacitor as discussed in section 2.

Electron columns may have an asymmetric engagement of additional lenses. For example if an additional lens is engaged at $10\,000\,X$ when increasing in magnification, it may not disengage until $8000\,X$ when decreasing in magnification. Because of the asymmetry, particular care is required to study the influence of magnifications when lens engagement boundaries are crossed [34]. Images collected in this work were always approached from lower magnification when a boundary was crossed (if a relay was audible) to avoid the effect. There is an audible relay engagement between $2500\,X$ and $5000\,X$, potentially explaining the slower response time of the system at the higher magnification, even though a smaller current impulse is required to scan the beam between to pixels.

When the microscope is not allowed to fully stabilize within the pixel dwell time, the detector response includes signals from multiple grid points along the beam settling path, as shown in Figure 10. The correction algorithms presented in Section 4.4 to shift and align the sampled image stack will be less effective for these shorter dwell times, since the reference signal (final pixel sample) is not a stabilized image. Artifacts in snake scan patterns can be fully mitigated and the system response measured by computing shifts with respect to neighboring rows of the same sample instead of the final sample of the same row. Raster scans can be corrected with the algorithm as presented, but the system response time can not be measured.
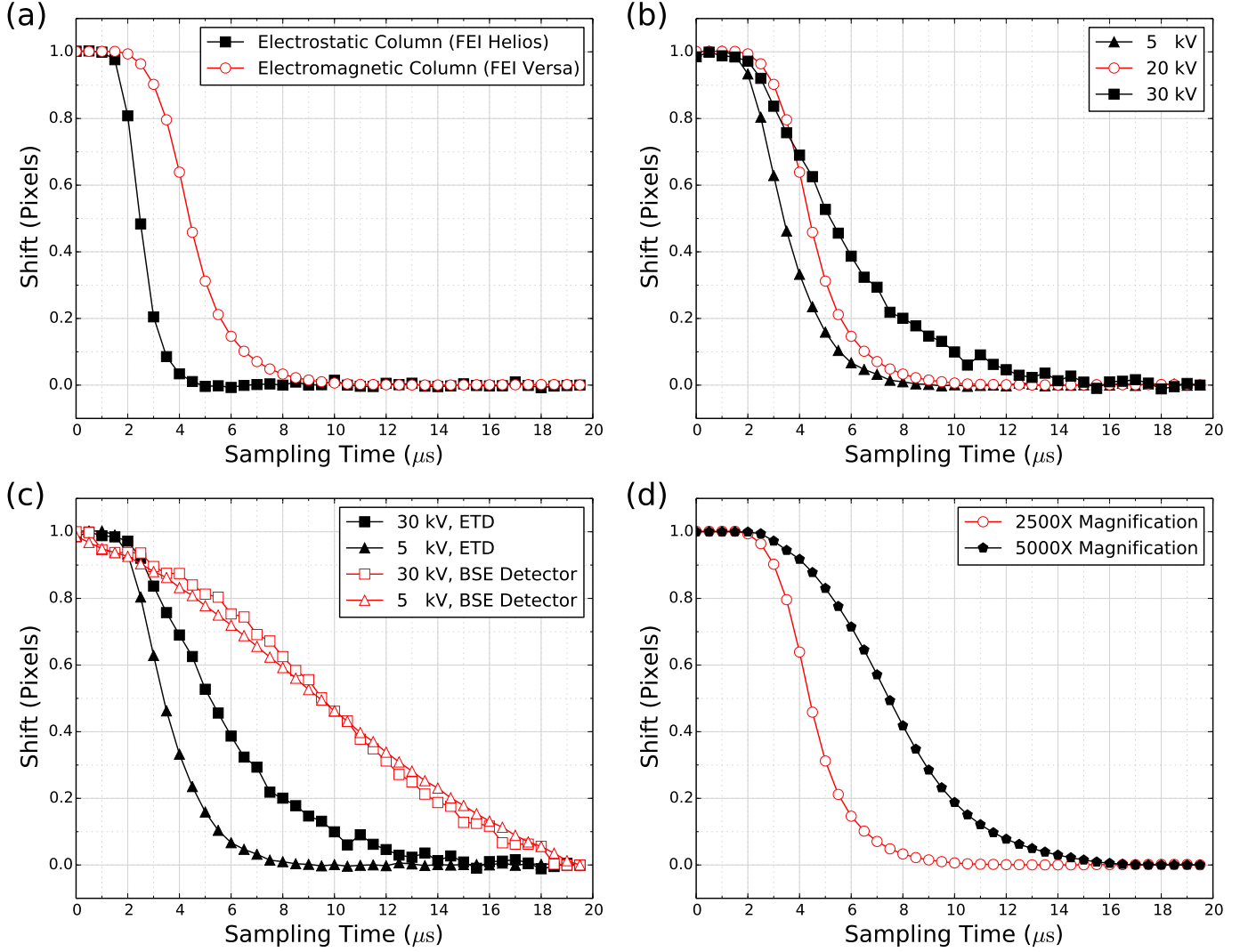
Figure 8: Relative pixel shifts as a function of time are shown for a range of beam parameters and detector types. (a) An identical microstructural region was imaged on two different SEM microscopes with the custom scan controller and identical imaging conditions, one with electromagnetic deflectors in the column and one with electrostatic deflectors in the column. The electrostatic column was observed to stabilize imaging twice as fast as the electromagnetic one. The electrostatic column stabilization time converges around 3–4 μs, whereas the electromagnetic column response time is 5–10 μs. (b) Beam accelerating voltage affected system stabilization time, with low kV being the fastest. (c) The system response time with a BSE detector is approximately twice as slow compared to the ETD, converging at or above a 20 μs dwell time. (d) The response time also depends on imaging magnification, with the settling time increasing at higher magnifications.

Uncorrected

Corrected

1 µs

(a) 400 nm

(b) 400 nm

10 µs
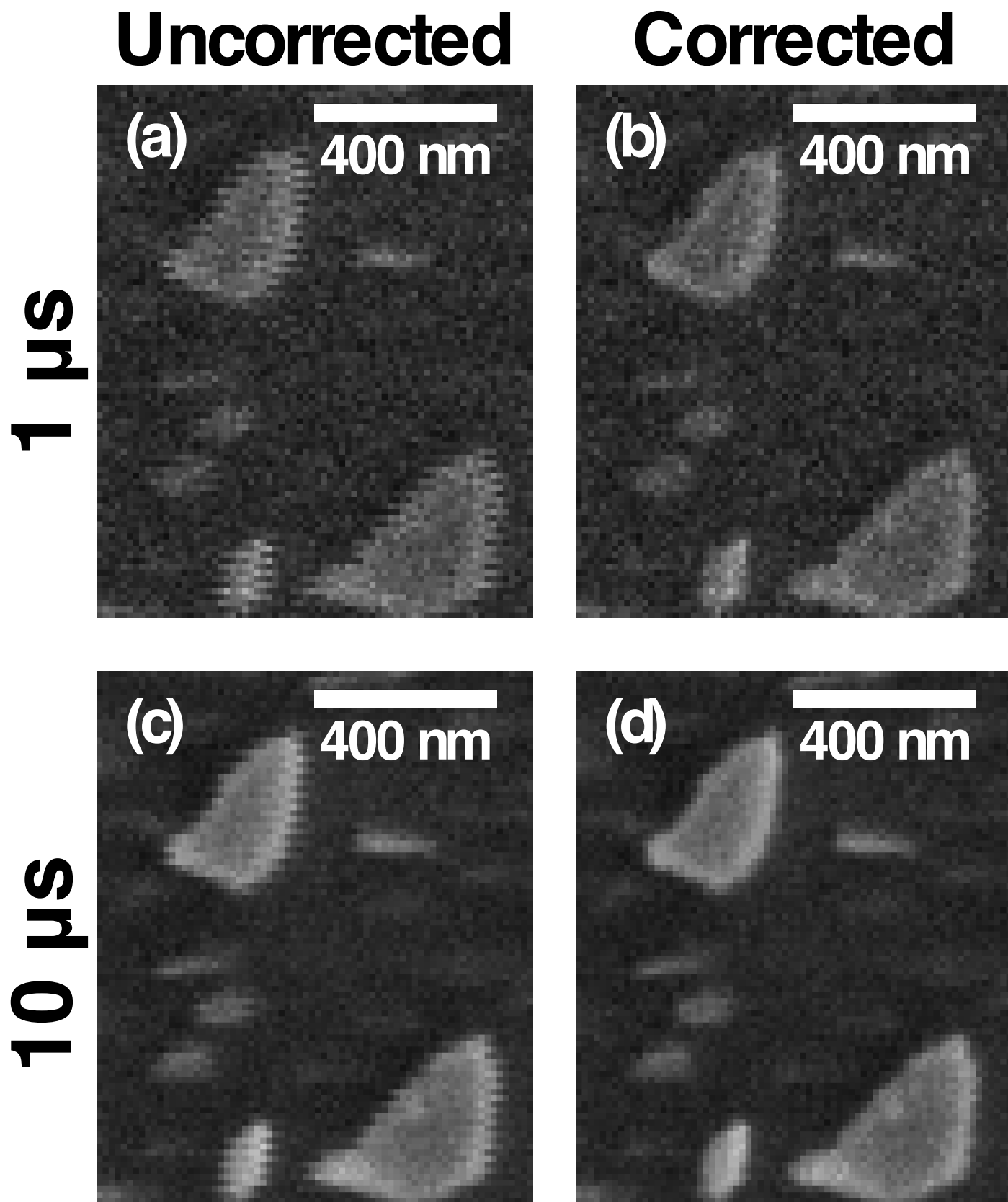
(c) 400 nm

(d) 400 nm

Figure 9: A datastack of detector sampling information was gathered using the custom IO controller from an etched Ti-6Al-4V sample. Imaging was performed for a total dwell of 1 µs and 10 µs, which are shown for both the raw (uncorrected) images that are averaged over the prescribed dwell time and corrected images, which were aligned and then averaged using the algorithm described in Section 4.4.
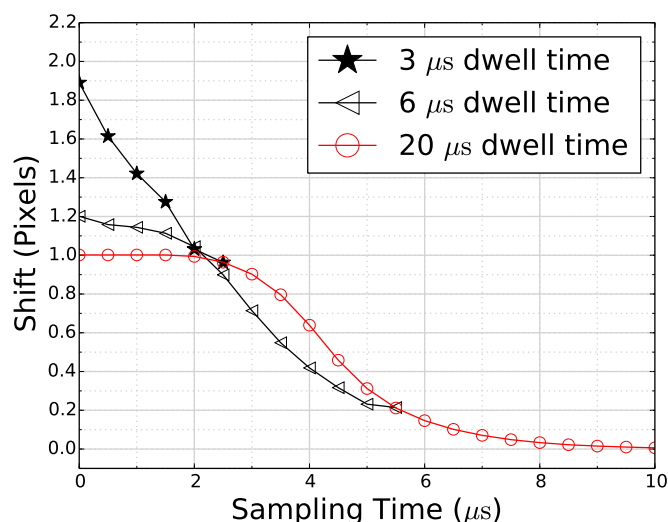
Figure 10: At short pixel dwell times, which are smaller than the stabilization time, the beam displacements can be larger than the distance between the current and previous requested beam location. This effect is often not noticeable due to a systematic shift in the entire imaging field of view. Shorter dwell times have been vertically shifted so the final sample intersects the 20 μs curve.

5. Conclusions

A custom beam scan and fast-sampling detector IO controller were implemented to improve image quality and to study the hardware components and SEM operating conditions that influence microscope stabilization time during beam scanning. External scan generation significantly reduces the magnitude of line jump errors and methods for correcting the scanning defects are presented, permitting improved SEM DIC imaging conditions. For high resolution imaging, pixel-scaled improvements in edge sharpness are obtained with the custom scan controller, which translate to μm-scaled particle edge sharpness improvements in the metals investigated.

In summary:

- The following variables influence the beam stabilization time or detector response time, which impact imaging quality: electron beam accelerating voltage (kV), detector type, column deflector type and hardware, and SEM magnification.

- The timescale for system stabilization, which is comprised of detector response time and the electron beam stabilizing to the desired position, is on the order of typical dwell times used for imaging (1–10 μs).

- External scan control provides a method for high resolution, fast sampling, and synchronized analog scan generation and detector signal acquisition, permitting time resolved sampling of detector signals and improved beam positioning precision.

- Preserving time-resolved fast sampling detector signal measurements enables measurement of and correction for beam and detector response delays present in any scan controller.

- Correcting for beam scanning stabilization artifacts improves spatial resolution by aligning detector samples.

References

[1] P. G. Callahan, J. C. Stinville, E. R. Yao, M. P. Echlin, M. S. Titus, M. D. Graef, D. S. Gianola, T. M. Pollock, Transmission scanning electron microscopy: Defect observations and image simulations, Ultramicroscopy 186 (2018) 49 – 61. doi:https://doi.org/10.1016/j.ultramic.2017.11.004.
http://www.sciencedirect.com/science/article/pii/S0304399117303315

[2] J. Holm, R. R. Keller, Acceptance angle control for improved transmission imaging in an SEM, Microscopy Today 25 (2) (2017) 12–19.

[3] P. Hawkes, Advances in Imaging and Electron Physics, no. v. 171 in Advances in Imaging and Electron Physics, Elsevier Science, 2012.
https://books.google.com/books?id=qygiGS4YhgcC

[4] J. C. Stinville, N. Vanderesse, F. Bridier, P. Bocher, T. M. Pollock, High resolution mapping of strain localization near twin boundaries in a nickel-based superalloy, Acta Materialia 98 (2015) 29–42. doi:10.1016/j.actamat.2015.07.016.
http://dx.doi.org/10.1016/j.actamat.2015.07.016

[5] A. D. Kammers, S. Daly, Self-Assembled Nanoparticle Surface Patterning for Improved Digital Image Correlation in a Scanning Electron Microscope, Experimental Mechanics 53 (8) (2013) 1333–1341. doi:10.1007/s11340-013-9734-5.

[6] M. A. Sutton, N. Li, D. C. Joy, A. P. Reynolds, X. Li, Scanning electron microscopy for quantitative small and large deformation measurements part i: Sem imaging at magnifications from 200 to 10,000, Experimental Mechanics 47 (6) (2007) 775–787. doi:10.1007/s11340-007-9042-z.
https://doi.org/10.1007/s11340-007-9042-z

[7] M. A. Sutton, N. Li, D. Garcia, N. Cornille, J. J. Orteu, S. R. McNeill, H. W. Schreier, X. Li, A. P. Reynolds, Scanning electron microscopy for quantitative small and large deformation measurements part ii: Experimental validation for magnifications from 200 to 10,000, Experimental Mechanics 47 (6) (2007) 789–804. doi:10.1007/s11340-007-9041-0.
https://doi.org/10.1007/s11340-007-9041-0

[8] J. Tracy, A. Waas, S. Daly, A new experimental approach for in situ damage assessment in fibrous ceramic matrix composites at high temperature, Journal of the American Ceramic Society 98 (6) (2015) 1898–1906. doi:10.1111/jace.13538.
http://dx.doi.org/10.1111/jace.13538

[9] E. Alabort, P. Kontis, D. Barba, K. Dragnevski, R. Reed, On the mechanisms of superplasticity in Ti-6Al-4V, Acta Materialia 105 (Supplement C) (2016) 449 – 463. doi:https://doi.org/10.1016/j.actamat.2015.12.003.
http://www.sciencedirect.com/science/article/pii/S1359645415301105

[10] I. Dastidar, V. Khademi, T. Bieler, A. Pilchak, M. Crimp, C. Boehlert, The tensile and tensile-creep deformation behavior of Ti-8Al-1Mo-1V(wt%), Materials Science and Engineering: A 636 (Supplement C) (2015) 289 – 300. doi:https://doi.org/10.1016/j.msea.2015.03.059.
http://www.sciencedirect.com/science/article/pii/S0921509315003019

[11] J. L. Carter, M. W. Kuper, M. D. Uchic, M. J. Mills, Characterization of localized deformation near grain boundaries of superalloy rené-104 at elevated temperature, Materials Science and Engineering: A 605 (2014) 127 – 136. doi:https://doi.org/10.1016/j.msea.2014.03.048.
http://www.sciencedirect.com/science/article/pii/S0921509314003177

[12] S. Maraghechi, J. P. Hoefnagels, R. H. Peerlings, M. G. Geers, Correction of scan line shift artifacts in scanning electron microscopy: An extended digital image correlation framework, Ultramicroscopy 187 (2018) 144–163.

[13] R. Jiang, F. Pierron, S. Octaviani, P. Reed, Characterisation of strain localisation processes during fatigue crack initiation and early crack propagation by sem-dic in an advanced disc alloy, Materials Science and Engineering: A 699 (2017) 128–144. doi:https://doi.org/10.1016/j.msea.2017.05.091.
http://www.sciencedirect.com/science/article/pii/S0921509317307074

[14] J. C. Stinville, M. Echlin, D. Texier, F. Bridier, P. Bocher, T. Pollock, Sub-grain scale digital image correlation by electron microscopy for polycrystalline materials during elastic and plastic deformation, Experimental Mechanics (2015) 1–20doi:10.1007/s11340-015-0083-4.
http://dx.doi.org/10.1007/s11340-015-0083-4

[15] K. Suzuki, S. Matsui, Y. Ochiai, Sub-Half-Micron Lithography for ULSIs, Cambridge University Press, 2000.
https://books.google.com/books?id=qgm8yzqgLO0C

[16] P. Hawkes, J. Spence, Science of Microscopy, Springer New York, 2008.
https://books.google.com/books?id=39aSIA7BufYC

[17] T. E. Everhart, R. F. M. Thornley, Wide-band detector for micro-microampere low-energy electron currents, Journal of Scientific Instruments 37 (7) (1960) 246.
http://stacks.iop.org/0950-7671/37/i=7/a=307

[18] E. D. Wolf, T. E. Everhart, Electron beam channeling in single crystal silicon by scanning electron microscopy, Applied Physics Letters 14 (10) (1969) 299–300. arXiv:https://doi.org/10.1063/1.1652657, doi:10.1063/1.1652657.
https://doi.org/10.1063/1.1652657

[19] J. Stephen, B. J. Smith, D. C. Marshall, E. M. Wittam, Applications of a semiconductor backscattered electron detector in a scanning electron microscope, Journal of Physics E: Scientific Instruments 8 (7) (1975) 607.
http://stacks.iop.org/0022-3735/8/i=7/a=021

[20] G. E. Lloyd, Atomic number and crystallographic contrast images with the SEM: a review of backscattered electron techniques, Mineralogical Magazine 51 (359) (1987) 3–19.

[21] X. Sang, J. M. LeBeau, Characterizing the response of a scintillator-based detector to single electrons, Ultramicroscopy 161 (2016) 3 – 9. doi:https://doi.org/10.1016/j.ultramic.2015.11.008.
https://www.sciencedirect.com/science/article/pii/S0304399115300735

[22] D. B. Williams, C. B. Carter, The transmission electron microscope, in: Transmission electron microscopy, Springer, 1996, pp. 3–17.

[23] J. Goldstein, D. Newbury, J. Michael, N. Ritchie, J. Scott, D. Joy, Scanning Electron Microscopy and X-Ray Microanalysis, Springer New York, 2017.
https://books.google.com/books?id=D0I_DwAAQBAJ

[24] D. D. Krueger, R. D. Kissinger, R. G. Menzies, Development and introduction of a damage tolerant high temperature nickel-base disk alloy, René88DT, Superalloy 1992 (1992) 277.

[25] W. C. Lenthe, J. C. Stinville, M. P. Echlin, T. M. Pollock, Statistical assessment of fatigue-initiating microstructural features in a polycrystalline disk alloy, in: Superalloys 2016: Proceedings of the 13th Intenational Symposium of Superalloys, Wiley Online Library, 2016, pp. 569–577.

[26] J. C. Stinville, M. P. Echlin, P. G. Callahan, V. M. Miller, D. Texier, F. Bridier, P. Bocher, T. M. Pollock, Measurement of strain localization resulting from monotonic and cyclic loading at 650°C in nickel base superalloys, Experimental Mechanics 57 (8) (2017) 1289–1309. doi:10.1007/s11340-017-0286-y.
https://doi.org/10.1007/s11340-017-0286-y

[27] M. P. Echlin, J. C. Stinville, V. M. Miller, W. C. Lenthe, T. M. Pollock, Incipient slip and long range plastic strain localization in microtextured Ti-6Al-4V titanium, Acta Materialia 114 (Supplement C) (2016) 164 – 175. doi:https://doi.org/10.1016/j.actamat.2016.04.057.
http://www.sciencedirect.com/science/article/pii/S1359645416303251

[28] J. Stinville, M. Echlin, D. Texier, F. Bridier, P. Bocher, T. Pollock, Sub-grain scale digital image correlation by electron microscopy for polycrys-

talline materials during elastic and plastic deformation, Experimental Mechanics 56 (2) (2016) 197–216. doi:10.1007/s11340-015-0083-4.
https://doi.org/10.1007/s11340-015-0083-4

[29] A. D. Kammers, S. Daly, Digital image correlation under scanning electron microscopy: methodology and validation, Experimental Mechanics 53 (9) (2013) 1743–1761.

[30] M. Guizar-Sicairos, S. T. Thurman, J. R. Fienup, Efficient subpixel image registration algorithms, Opt. Lett. 33 (2) (2008) 156–158. doi:10.1364/OL.33.000156.
http://ol.osa.org/abstract.cfm?URI=ol-33-2-156

[31] Correlated Solution Inc., Vic-2D Software 2009, Colombia, SC.

[32] A. D. Kammers, S. Daly, Small-scale patterning methods for digital image correlation under scanning electron microscopy, Measurement Science and Technology 22 (12) (2011) 125501. doi:10.1088/0957-0233/22/12/125501.
http://iopscience.iop.org/0957-0233/22/12/125501

[33] M. A. Sutton, J. J. Orteu, H. Schreier, Image Correlation for Shape, Motion and Deformation Measurements: Basic Concepts, Theory and Applications, Springer Science & Business Media, 2009.

[34] A. W. Mello, T. A. Book, A. Nicolas, S. E. Otto, C. J. Gilpin, M. D. Sangid, Distortion correction protocol for digital image correlation after scanning electron microscopy: Emphasis on long duration and ex-situ experiments, Experimental Mechanics 57 (9) (2017) 1395–1409. doi:10.1007/s11340-017-0303-1.
https://doi.org/10.1007/s11340-017-0303-1

Microscope Response Time

Shift (Pixels) vs Sampling Time (μs)

Uncorrected

Corrected